European Journal of Pharmaceutics and Biopharmaceutics 137 (2019) 175–184

Contents lists available at ScienceDirect

European Journal of Pharmaceutics and Biopharmaceutics

journal homepage: www.elsevier.com/locate/ejpb

Research paper

# Octa-arginine boosts the penetration of elastin-like polypeptide nanoparticles in 3D cancer models

Lisanne M.P.E. van Oppen[a,c,1], Jan Pille[b,d,1], Christiaan Stuut[a], Marleen van Stevendaal[a,b], Lisa N. van der Vorm[a], Jan A.M. Smeitink[c], Werner J.H. Koopman[a], Peter H.G.M. Willems[a], Jan C.M. van Hest[b,d], Roland Brock[a,*]

[a] Department of Biochemistry, Radboud Institute for Molecular Life Sciences (RIMLS), Radboud University Medical Center, PO Box 9101, 6500 HB Nijmegen, the Netherlands
[b] Department of Biomedical Engineering & Department of Chemical Engineering and Chemistry, Eindhoven University of Technology, PO Box 513, 5600 MB Eindhoven, the Netherlands
[c] Department of Pediatrics, Radboud Center for Mitochondrial Medicine, Radboud University Medical Center, Geert Grooteplein Zuid 10, PO Box 9101, 6500 HB Nijmegen, the Netherlands
[d] Department of Bio-Organic Chemistry, Institute for Molecules and Materials, Radboud University, Heyendaalseweg 135, PO Box 9010, 6525 AJ Nijmegen, the Netherlands

ARTICLE INFO

*Keywords:*
Elastin-like polypeptide nanoparticles
Octa-arginine
Penetration
Binding site barrier
Spheroid

ABSTRACT

Elastin-like polypeptide (ELP) nanoparticles are a versatile platform for targeted drug delivery. As for any type of nanocarrier system, an important challenge remains the ability of deep (tumor) tissue penetration. In this study, ELP particles with controlled surface density of the cell-penetrating peptide (CPP) octa-arginine (R8) were created by temperature-induced co-assembly. ELPs formed micellar nanoparticles with a diameter of around 60 nm. Cellular uptake in human skin fibroblasts was directly dependent on the surface density of R8 as confirmed by flow cytometry and confocal laser scanning microscopy. Remarkably, next to promoting cellular uptake, the presence of the CPP also enhanced penetration into spheroids generated from human glioblastoma U-87 cells. After 24 h, uptake into cells was observed in multiple layers towards the spheroid core. ELP particles not carrying any CPP did not penetrate. Clearly, a high CPP density exerted a dual benefit on cellular uptake and tissue penetration. At low nanoparticle concentration, there was evidence of a binding site barrier as observed for the penetration of molecules binding with high affinity to cell surface receptors. In conclusion, R8-functionalized ELP nanoparticles form an excellent delivery vehicle that combines tunability of surface characteristics with small and well-defined size.

## 1. Introduction

The encapsulation of drugs into nanoparticles is gaining significance in targeted drug delivery for achieving a higher drug dose at the site of action and for increasing the bioavailability of drugs with poor water solubility. At this point, liposomes are still the most widely used drug carriers [1]. Alternatively, nanoparticles made from a great variety of polymers are being explored [2]. For systemic application, biodegradability or elimination through excretion are important prerequisites. As a consequence, a major focus so far has been on polyester-based polymers such as the polylactic acid co-glycolides (PLGAs) or polycaprolactones [3].

Protein-based nanoparticles are being pursued as a further strategy [4,5]. In the same way as polyesters, these polyamides can also be degraded into non-toxic natural building blocks. However, in comparison to synthetic polymers, for the formation of nanoparticles, very different boundary conditions apply. For synthetic polymers, nanoparticle formation typically occurs by hydrophobic collapse, once a solution of organic solvent, containing the polymer, is diluted into an aqueous phase. For recombinant proteins whose intact tertiary structure defines functionality, this approach is not possible. They often have to be water soluble in their monomeric form in order to achieve high expression yields and purification.

Elastin-like polypeptides (ELPs) are derived from human

* Corresponding author at: Dept. of Biochemistry (286), Radboud Institute for Molecular Life Sciences, Radboudumc, Geert Grooteplein 28, 6525 GA Nijmegen, The Netherlands.
*E-mail address:* roland.brock@radboudumc.nl (R. Brock).
[1] Authors contributed equally to this research.

https://doi.org/10.1016/j.ejpb.2019.02.010
Received 23 October 2018; Received in revised form 22 December 2018; Accepted 14 February 2019
Available online 15 February 2019
0939-6411/ 

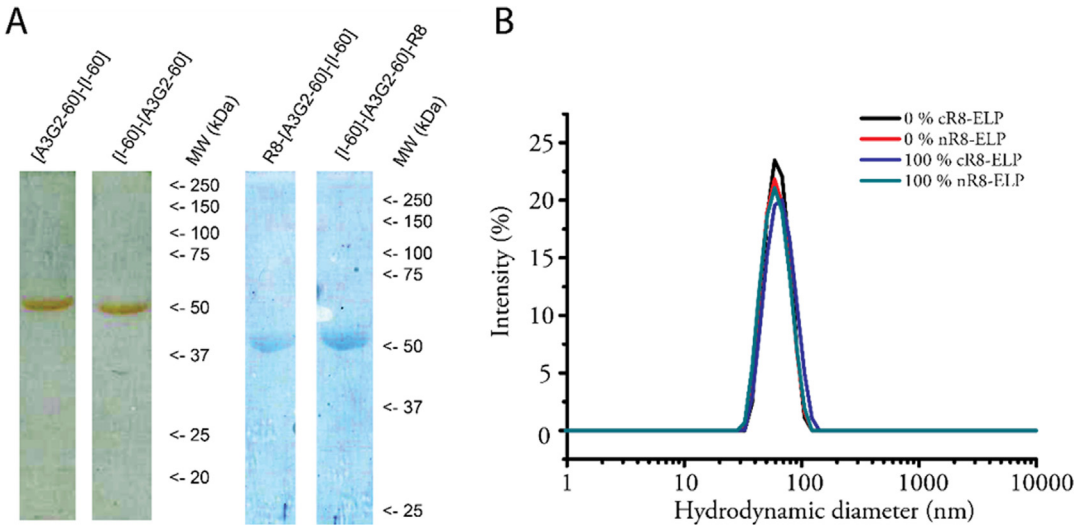


**Fig. 1.** Characterization of ELPs and ELP nanoparticles. (A) SDS-Page of c-ELP, n-ELP (silver-stained) and cR8-ELP, nR8-ELP (coomassie-stained); (B) dynamic light scattering results of particles consisting of 0% or 100% cR8-ELP and nR8-ELP, respectively.

tropoelastin, a precursor of elastin, a component of the extracellular matrix [4,6]. ELPs consist of pentameric repeats of GXGVP, where the guest residue (X) can be any naturally occurring amino acid [7,8]; ELPs with unnatural amino acids have been reported as well [9]. These polymers show a reversible, temperature-dependent self-organization into coacervates. Upon raising the temperature above the lower critical solution temperature (LCST), they undergo a shape transition from a disordered, soluble state to a spiral-like state consisting of type-II β-turns, type-I β-turns and β-strands, exposing the (hydrophobic) side chains [10]. This aggregation is thermodynamically driven. By changing the guest residue or length of the polymer it is possible to tune the LCST of ELPs [11,12]. To direct this aggregation towards the formation of well-defined nanoparticles, diblock ELPs were designed with a hydrophilic ELP sequence (high LCST) and with a hydrophobic ELP sequence (low LCST) that differ in their guest residues. Between the two respective LCSTs these diblock ELPs exist as micellar structures.

ELP-based nanoparticles hold great potential for drug delivery [13–18]. Drugs can be encapsulated either into the hydrophilic lumen or into the hydrophobic coacervate shell, or via covalent coupling. In addition, ELPs can be extended by functional peptides to achieve cell-specific targeting or enhance cellular uptake [19]. As a means to enhance cellular uptake, cell-penetrating peptides (CPPs) are widely employed. CPPs are mostly cationic peptides of 8–30 amino acids in length that induce the cellular uptake of (macro-) molecules that otherwise only poorly enter cells [20]. This capacity also extends to nanoparticles [21]. Arginine-rich CPPs are a prominent class of CPPs. Oligoarginines between 6 and 12 arginine residues show optimal activity as CPPs [22]. Interestingly, for functionalization of nanoparticles, multivalency afforded by coupling of many individual arginine building blocks shows less activity than coupling of an equivalent number of arginines in the form of oligopeptides [23]. Very clearly, the structural arrangement of the arginine residues also plays a role [24]. For nanoparticles, CPP density has a positive impact on uptake [25].

To this point, the major part of CPP research has focused on delivery in two-dimensional tissue cultures. Very clearly, this setting bears little resemblance with the *in vivo* situation, where drug delivery systems need to penetrate tissues in three dimensions. In 3D, particle size is a critical parameter. Moreover, particle binding and porosity of tissue are key factors in effective nanoparticle treatment [26,27]. For drug delivery systems that employ active targeting through incorporation of receptor ligands, the binding site barrier (BSB) effect can compromise penetration [28,29]. High-affinity binding leads to capture of ligand-functionalized particles in the periphery of the cell mass. Further entry is a function of successive saturation of binding sites from the periphery, as demonstrated *in vivo* by Lee et al. [30]. Arginine-rich CPPs interact with the heparan sulfate proteoglycans of the glycocalyx. While each individual CPP binds with affinities in the lower micromolar to higher nanomolar range a polyvalent presentation may strongly increase interactions due to avidity effects [31].

Here, we investigated the impact of CPP density on penetration of ELP nanoparticles in 3D cancer cell spheroids. Spheroids are excellent models for avascular regions of tumor tissue and can be generated with a highly reproducible morphology thus enabling a reliable determination of particle penetration [27]. In particular, we were interested to learn whether a higher CPP density, which should yield more efficient uptake in 2D, would compromise penetration in 3D due to sequestration of particles in the outer cell layer.

Nanoparticles of around 60 nm were formed with an ELP diblock copolymer. Octa-arginine density was varied by incorporating different molar fractions of ELP elongated with the CPP. To determine cellular uptake and localization in 2 and 3 dimensions, Alexa$^{647}$ was incorporated as a fluorophore. In 2D, uptake was a direct function of CPP density. Interestingly, in 3D CPP density benefitted penetration, as well.

## 2. Results

### 2.1. Characterization of ELP nanoparticles

ELPs consisted of a hydrophilic block [A3G2-60] (60 GXGVP pentarepeats with alanine and glycine as the guest residue X in a ratio of 3:2) and a hydrophobic block [I-60] (60 GXGVP pentarepeats with isoleucine as the guest residue X) (see Supplementary Information for sequences). To assess whether the orientation of the terminus with respect to the blocks had an impact on particle formation and uptake, ELPs were expressed with the hydrophilic block either at the N-terminus (n-ELP) or at the C-terminus (c-ELP). Either variant was extended with octa-arginine (R8) at the hydrophilic, outer block yielding nR8-ELP and cR8-ELP. Proteins were expressed and purified with yields ranging between 20 and 100 mg/L bacterial culture (Fig. 1A). Masses measured by electrospray ionization – time of flight (ESI-TOF) mass spectrometry corresponded well to the theoretical values after cleavage of the N-terminal formylmethionine (Fig. S1 and Table 1). ELP nanoparticles (10 μM) were formed through self-organization by shifting the temperature from 4 to 37 °C, exceeding the LCST of the hydrophobic block [I-60] (22 °C). Dynamic light scattering (DLS) at physiological conditions showed monodisperse particles with a diameter of ~60 nm

**Table 1**
Overview of proteins used in this study.

| Protein | Theoretical mass (Da)[a] | Measured mass (Da)[b] | Hydrodynamic diameter (nm)[c] |
|---|---|---|---|
| c-ELP | 48,198 | 48,198 | 60.5 ± 8.8 |
| n-ELP | 48,198 | 48,198 | 58.7 ± 10.3 |
| cR8-ELP | 49,505 | 49,503 | 63.0 ± 15.7 |
| nR8-ELP | 49,505 | 49,504 | 58.0 ± 13.2 |

[a] The theoretical mass was determined with ExPASy (http://www.expasy.org/) excluding the N-terminal methionine.
[b] Mass found after deconvolution of the mass spectrum.
[c] Values are represented as mean ± SD from three independent measurements.

for all four ELP variants (Fig. 1B, Table 1). These data indicate that neither the position of the hydrophilic block within the ELP diblock copolymer nor its extension with R8 had an effect on the formation and size of the ELP nanoparticles.

### 2.2. Uptake of ELP-R8 nanoparticles directly correlates with CPP density

First, we determined the dependence of the increase in cell-associated fluorescence on the position of the hydrophilic block and the R8 density on the surface of Alexa$^{647}$-labeled ELP nanoparticles using primary human skin fibroblasts. To this end, ELP nanoparticles were formed without and with increasing percentages of N-terminal R8-ELP (nR8-ELP) by mixing n-ELP and nR8-ELP monomers in different ratios. A fixed ratio (5%) of Alexa$^{647}$-labeled ELP was incorporated for detection of fluorescence (Fig. S2). Nanoparticles were added to the cell culture medium at a final ELP monomer concentration of 10 μM.

After two hours of incubation cellular uptake and subcellular distribution were determined by flow cytometry and confocal laser scanning microscopy. Cell-associated fluorescence showed a strong linear increase with the ratio of nR8-ELP in the particles (Fig. 2A). This dependence of uptake was independent of the orientation of the CPP on the ELP, as C-terminal R8-ELP (cR8-ELP) showed a similar dependence on incorporated R8-ELP. However, at lower percentages of R8 (0–25%) cellular uptake tended to be lower for cR8-ELP than for nR8-ELP (no statistical significant differences). In the remainder of this study we used n-ELP based nanoparticles.

Whether cell-associated fluorescence reflected particles taken up into cells was investigated with confocal laser scanning microscopy. As for flow cytometry, only little cell-associated fluorescence was observed for ELP nanoparticles not containing any CPP. At 5% nR8-ELP, the total fluorescence was localized inside cells. At 50% nR8-ELP, fluorescence accumulated at the plasma membrane which was even more prominent at 90% (Fig. 2B).

This cellular uptake of ELP nanoparticles showed a strong time-dependence. After one hour of incubation with 10% nR8-ELP nanoparticles, fluorescence was primarily observed at the plasma membrane. After two hours, particles were taken up and showed partial overlap with acidic vesicular structures as evident from colocalization with lysotracker. This colocalization further increased towards four hours (Fig. 2C).

To obtain information about the endocytotic pathways that are involved in the uptake of the nR8-ELP nanoparticles, macropinocytosis, caveolae-mediated endocytosis and clathrin-mediated endocytosis were inhibited with their respective inhibitors amiloride (50 μM), genistein (100 μM) and monodansylcadaverine (50 μM). Cells were incubated for 2 h with n-ELP nanoparticles containing the indicated percentages of nR8-ELP, added at a final monomer concentration of 10 μM, in the absence and presence of inhibitor. The mean cellular fluorescence intensity was measured by flow cytometry and for each percentage of nR8-ELP the value obtained with the untreated control was set at 100% to which the inhibitor values were related. Up to 10% nR8-ELP, all three inhibitors reduced the mean cellular fluorescence intensity with amiloride being more effective than the other two inhibitors (Fig. S3). The inhibitory effect of amiloride, but not that of the other two inhibitors, was also observed at the higher percentages (greater than 10%) of nR8-ELP. Based on the observation that at 5% nR8-ELP all cell-associated fluorescence was localized to intracellular punctate structures (Fig. 2B), we conclude that macropinocytosis is the predominant uptake process of nR8-ELP nanoparticles.

### 2.3. R8-ELP nanoparticles are non-toxic up to 25% R8

The accumulation of ELP nanoparticles at 50% nR8-ELP and higher at the plasma membrane could cause disturbance of membrane integrity. To investigate the potential toxicity of ELP nanoparticles, we measured propidium iodide (PI) positive cells as a hallmark of plasma membrane damage and necrosis [32]. The percentage of affected cells for concentrations of 0.5–10 μM ELP monomers was similar to the one of untreated cells, regardless of the percentage nR8 included (Fig. 3). However, for concentrations of 50 μM ELP monomers and higher, significant cell death was observed for an nR8 content of 25% and higher. 10% nR8-ELP monomers were well tolerated even at a concentration of 100 μM.

### 2.4. Penetration of nR8-ELP nanoparticles into 3D tumor spheroids

The 2D experiments had shown a strong linear relationship of cell association/uptake and R8 density. Next, we were interested to learn to which degree the nR8-ELP nanoparticles had the capacity to penetrate 3D tumor spheroids and how penetration was influenced by the density of the CPP. On the one hand, a high CPP density could promote association of ELP nanoparticles with the spheroid and thus entry, on the other hand nanoparticles could be captured and retained in the periphery of the spheroid due to a binding site barrier.

Using *HeLa-Trex Flp-in Cox8 acGFP1* cells stably expressing a mitochondrially localized green fluorescent protein we first determined the capacity of standard confocal microscopy to penetrate the spheroid core. In this case, the GFP fusion protein only served as a cell tracer and the mitochondrial localization was without significance for our experiments. As expected for confocal microscopy, fluorescence could be detected into a penetration depth of up to 60 μm (Fig. S4A). However, only spheroids with diameters larger than 400–500 μm generally display the typical, layered structure consisting of a necrotic core, surrounded by viable quiescent cells and an outer layer of proliferating cells [33,34]. Because of the need to detect the signal of nanoparticles in the core of a spheroid at a distance of at least 200 μm from the periphery, we fixed and cut the spheroid in halves followed by confocal laser scanning microscopy of the equatorial plane. Fluorescence was homogenously distributed over the whole central area of the spheroid (Fig. S4B). Parallel to this strategy, we applied a clearing method adapted from Ke et al. for the visualization of the inner core of spheroids [35]. As clearing agent, high-concentration fructose solutions were used to reduce light scattering within spheroids (Fig. S4C).

In the remainder of this paper, we used spheroids grown from U-87 human glioblastoma cells as an *in vitro* 3D tumor model. To evaluate uptake and penetration capacity, U-87 spheroids were incubated for 5 h or 24 h with nR8-ELP nanoparticles (0%, 10% and 25% nR8) added at a final monomer concentration of 10 μM. At the end of the incubation period, spheroids were fixed and bisectioned after which a confocal image was taken of the equatorial plane. Exposure to the nanoparticles had no impact on spheroid morphology in terms of area (Fig. S5A) and aspect ratio (Fig. S5B). After an incubation time of 5 h, the ELP nanoparticles were hardly visible in the peripheral cell layers of the spheroid. Only little penetration was observed for 10% nR8-ELP nanoparticles, and a slight increase in penetration for 25% nR8-ELP nanoparticles (Fig. 4A, upper panel). In contrast, after 24 h there was a clear dependence of fluorescence and penetration depth on nR8-ELP

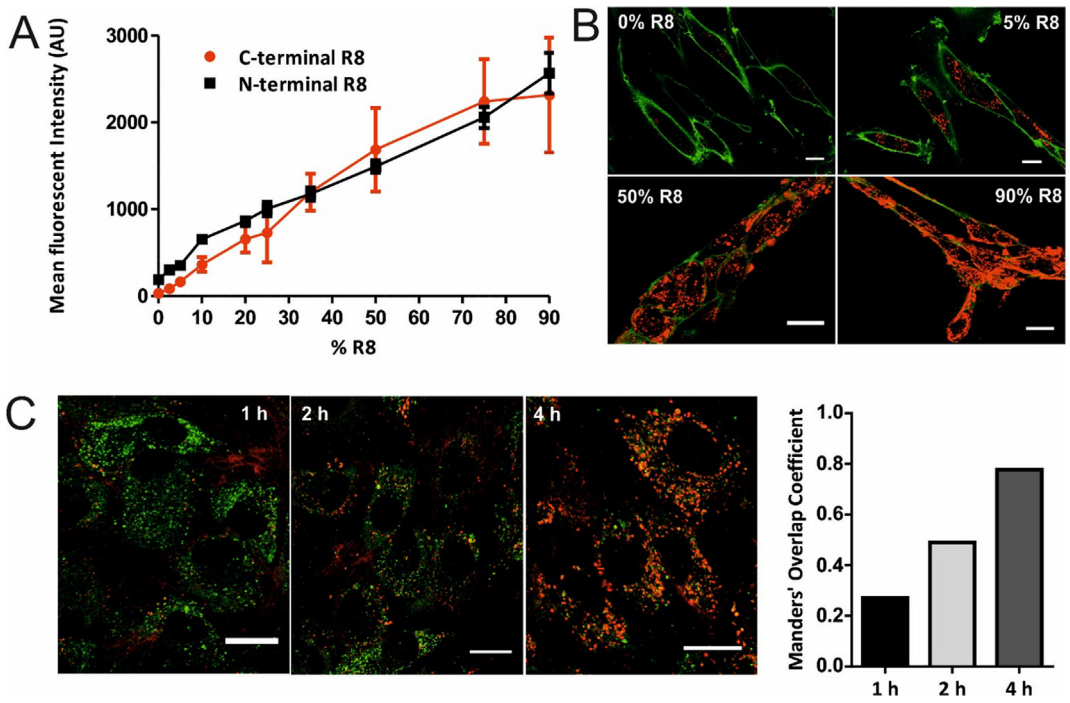


**Fig. 2.** Cellular uptake of ELP nanoparticles by primary human skin fibroblasts. (A) Mean fluorescence intensity of cells incubated for 2 h with nanoparticles containing Alexa$^{647}$-labeled c- or n-ELP without and with the indicated percentages of cR8- (red symbols) or nR8-ELP (black symbols) and added at a final monomer concentration of 10 μM. Mean cellular fluorescence intensity was quantified by flow cytometry. Values presented are the mean ± SEM of 3 independent experiments (red) or 2 independent experiments (black). Significance was assessed using two-way ANOVA followed by Bonferroni's multiple comparisons test (no significant differences). (B) Subcellular distribution of ELP-associated fluorescence (red) after 2 h incubation with n-ELP nanoparticles containing the indicated percentages of nR8-ELP and added at a final monomer concentration of 10 μM as revealed by confocal laser scanning microscopy. Plasma membranes were visualized by Cell Mask Green (green) (scale bars 20 μm). (C) Lysosomal localization of ELP associated fluorescence (red) after 1 h, 2 h, and 4 h incubation with 10% nR8-ELP nanoparticles added at a final monomer concentration of 10 μM. Acidic compartments were labeled with LysoTracker Green. ELP nanoparticles; red, lysosomes; green, scale bars 20 μm. Mander's Overlap Coefficient was calculated as a measure for colocalization (n = 1). (For interpretation of the references to colour in this figure legend, the reader is referred to the web version of this article.)

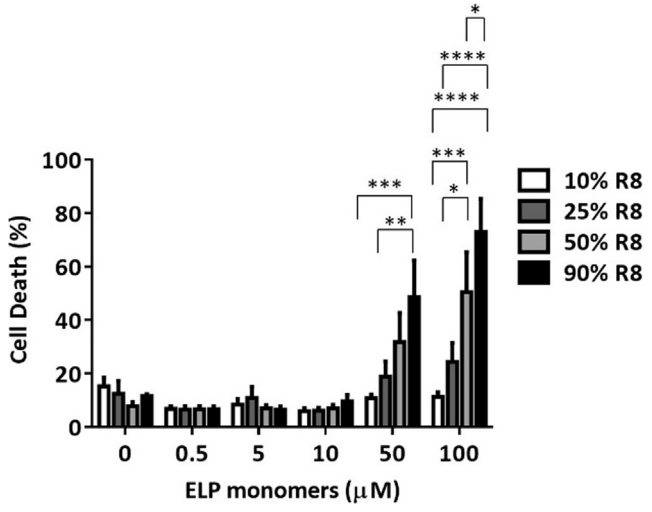


**Fig. 3.** Determination of nR8-ELP toxicity. Cell damage was determined via the fraction of propidium iodide positive fibroblasts (sub-G1 phase) after 24 h treatment with n-ELP nanoparticles containing the indicated nR8-ELP percentage and added at the indicated final monomer concentration. Error bars denote the standard error of the mean (SEM) of 3 independent experiments. Significance was assessed using two-way ANOVA, followed by Tukey's multiple comparisons test. Significant differences are indicated by $^{*}P < 0.05$, $^{**}P < 0.01$, $^{***}P < 0.001$, $^{****}P < 0.0001$.

content (Fig. 4A, lower panel). ELP nanoparticles containing 25% nR8-ELP displayed the highest fluorescence and the deepest penetration into the spheroid. The dot-like distribution of ELP nanoparticles indicated intracellular localization. This showed that on one hand the ELP nanoparticles functionalized with R8 were accumulated by cells as a result of the cell uptake-inducing effect of octa-arginine. On the other hand, the CPP also promoted penetration into the spheroids. This is reflected in the fluorescence intensity as function of the distance from the outer edge (0 μm) to the core (200 μm) in a mean radial intensity profile displaying average values every 10 μm (Fig. 4B). Interestingly, after normalization of the intensity profiles to the maximum fluorescence intensity at 20 μm from the outer edge, penetration for 10% and 25% nR8-ELP nanoparticles was nearly indistinguishable after 24 h incubation (Fig. 4C). Penetration depth of nR8-ELP nanoparticles after 5 h and 24 h incubation was independent of the size of the spheroids (Fig. S6).

To determine the extent of cellular uptake, U-87 spheroids were treated for 5 h and 24 h with n-ELP nanoparticles containing 0%, 10% or 25% nR8-ELP at a final monomer concentration of 10 μM. At the end of the incubation period, the spheroids were fixed and cut into halves. Subsequently, the nuclei and actin skeleton were stained after which a confocal image was taken at the equatorial plane. After an incubation time of 5 h, for 0% nR8-ELP nanoparticles no uptake was observed (Fig. 5). For 10% nR8-ELP nanoparticles after 5 h, a few faint dots were present in the cells of the outer layer of the spheroid. 25% nR8-ELP nanoparticles showed the strongest uptake. After 5 h, nanoparticles could be detected inside cells, three cell layers deep into the spheroid. After 24 h for 0% nR8-ELP nanoparticles hardly any uptake was observed. For 25% nR8-ELP nanoparticles extensive uptake was present five cell layers into the spheroid (~80 μm). The data show that along with penetration, a fraction of ELPs is taken up by the cells.

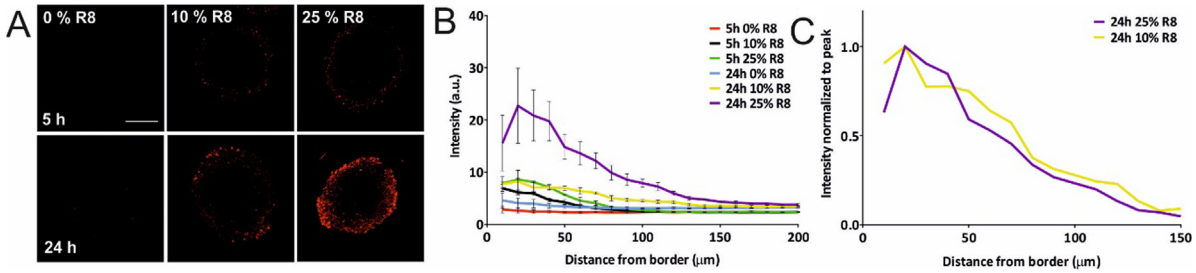


**Fig. 4.** Distribution of fluorescence of nR8-ELP nanoparticles (0%, 10%, and 25% nR8-ELP) in U-87 spheroids after 5 h and 24 h incubation at 10 μM final concentration of ELP monomers. (A) Visualization of penetration depth of nR8-ELP nanoparticles (0%, 10%, and 25% nR8-ELP) after 5 h (upper panel) and 24 h incubation (lower panel). The fluorescence intensity is visualized by confocal laser scanning microscopy of the equatorial plane of fixed and bisectioned spheroids. Scale bar is 200 μm. (B) The fluorescence intensity of the nR8-ELP nanoparticles (0%, 10%, and 25% nR8-ELP) in the spheroid after 5 h and 24 h incubation represented in a mean radial intensity profile. The average fluorescence was extracted every 10 μm represented the distance from the outer edge of the spheroid (0 μm) to the inner core (200 μm). Error bars denote the standard error of the mean (SEM) from two independent experiments, with at least two spheroids measured per condition per experiment. (C) Background corrected (minimal fluorescence intensity) fluorescence of 10% and 25% nR8-ELP nanoparticles after 24 h incubation, normalized to the maximum fluorescence intensity of the peak at 20 μm from the outer edge of the spheroid.

### 2.5. Concentration dependence of penetration depth

At this point, we wanted to learn whether penetration of 25% nR8-ELP nanoparticles after 24 h incubation was dependent on ELP concentration as this would indicate the presence of a binding site barrier, either due to cellular uptake or due to binding to the extracellular matrix. For both cases, ELP nanoparticles should penetrate deeper into the spheroids at higher concentrations. We tested three different concentrations of 25% nR8-ELP nanoparticles (2.5 μM, 10 μM and 25 μM). Penetration was determined after fixation and clearing. For a reliable extraction of quantitative information on penetration depth, we developed a method to measure the mean radial intensity profile of the distribution of ELP nanoparticles across the equatorial plane of spheroids (Custom program, SI). The highest concentration of 25 μM displayed consistently the highest intensities inside the spheroids (Fig. 6A). However, after normalization of the mean radial profiles of 2.5 μM and 10 μM 25% nR8-ELP nanoparticles to the maximum fluorescence intensity of the peak at 30 μm, both 10 μM and 25 μM displayed very similar intensity profiles, demonstrating that for these concentrations the penetration was independent of nanoparticle concentration (Fig. 6B). In contrast, for 2.5 μM 25% nR8 ELP nanoparticles fluorescence was only present in the periphery indicative of a binding site barrier.

### 2.6. nR8-ELP nanoparticles display highest penetration depth after 24 h

After the evaluation of concentration of ELP nanoparticles on penetration depth, we measured the impact of incubation time on penetration depth of 25 μM 25% nR8-ELP nanoparticles. U-87 spheroids were incubated with 25 μM 25% nR8-ELP nanoparticles varying from 0.5 h to 48 h and subsequently fixed and cleared. An incubation time of 24 h displayed the highest penetration depth (Fig. 7A). In the outer layers, fluorescence of ELP nanoparticles increased over time with a maximum at 4 h. When the incubation time was increased to 48 h, intensities decreased. This observation may be attributed to degradation of ELP nanoparticles. However, the coherence and regularity of spheroids decreased from 24 to 48 h, as well (Fig. S7). After normalization of the mean radial profiles for the different incubation times to maximum fluorescence intensities at 30 μm from the outer layer, the intensity profiles of 24 h and 48 h demonstrate high fluorescence intensities towards the central parts of the spheroid (Fig. 7B).

## 3. Discussion

Here, we show that functionalization of ELP nanoparticles with the cell-penetrating peptide (CPP) octa-arginine (R8) simultaneously conferred two functional characteristics which are highly relevant for future *in vivo* drug delivery applications. On the one hand, the CPP mediated the cellular uptake of the nanoparticles, on the other hand, the CPP also promoted the penetration of nanoparticles into 3D tumor spheroids. Both activities positively correlated with the density of the CPP on the surface of the nanoparticles.

By swapping the orientation of the hydrophilic and hydrophobic protein block, we evaluated both C-terminal (cR8-ELP nanoparticles) and N-terminal conjugation of the CPP (nR8-ELP nanoparticles). Uptake of nR8-ELP nanoparticles was slightly higher which may be attributed to the negatively charged C-terminus counteracting the positive charge of octa-arginine. Investigating the accompanying mechanism of uptake

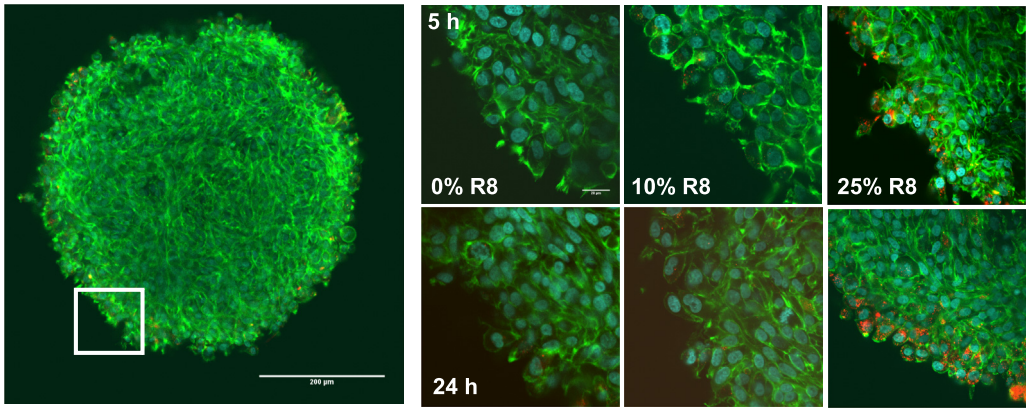


**Fig. 5.** Intracellular uptake of ELP nanoparticles in U-87 spheroids. Spheroids of similar size (400 μm) were incubated with ELP nanoparticles containing 0%, 10% or 25% of nR8-ELP for 5 h and 24 h and imaged by confocal laser scanning microscopy after fixation, sectioning and staining. The actin-cytoskeleton of the cells was stained with phalloidin (green) and the nucleus with DAPI (cyan) to evaluate the intracellular distribution. The box in the overview indicates the approximate size of the enlargements. Scale bar is 200 μm. (For interpretation of the references to colour in this figure legend, the reader is referred to the web version of this article.)

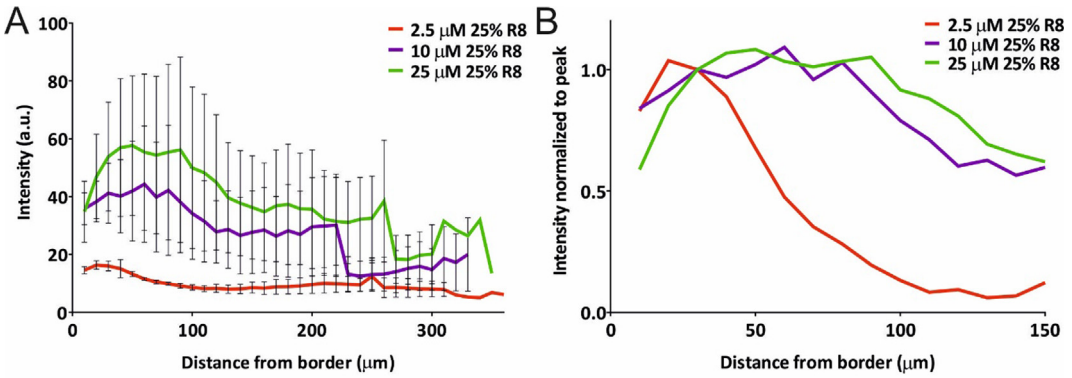


**Fig. 6.** Distribution of different concentrations of 25% nR8-ELP nanoparticles in cleared U-87 spheroids. (A) Mean radial intensity profiles at the equatorial plane of cleared U-87 spheroids for 2.5 μM, 10 μM and 25 μM Alexa$^{647}$-labeled 25% nR8-ELP nanoparticles after 24 h incubation. Values represented as mean of three independent experiments (three spheroids per experiment) ± SEM. (B) The fluorescence intensity of 2.5 μM, 10 μM and 25 μM nR8-ELP nanoparticles after 24 h incubation represented after background correction (minimal fluorescence intensity) and normalized to maximum fluorescence intensity of the peak at 30 μm from the outer edge of the spheroid.

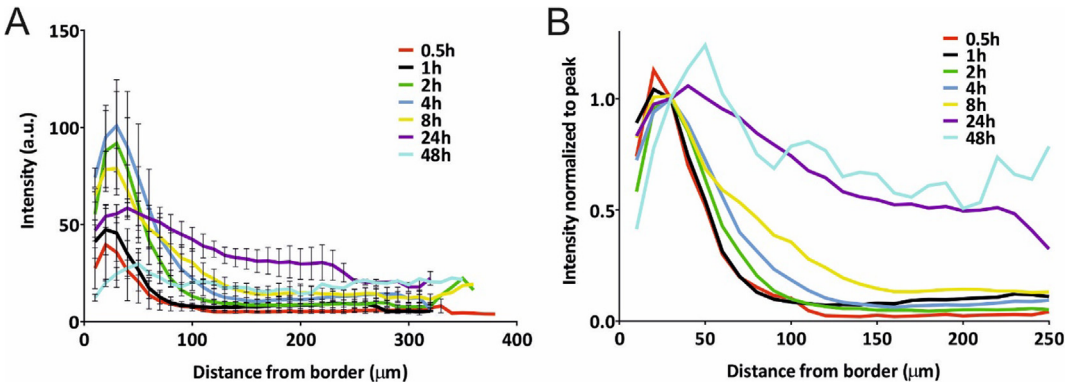


**Fig. 7.** Distribution of 25 μM 25% nR8-ELP nanoparticles in cleared U-87 spheroids after different incubation times (0.5–48 h). (A) Mean radial intensity profiles of the equatorial plane of cleared U-87 spheroids. Values represented as mean of three independent experiments (three spheroids per experiment) ± SEM (B) The fluorescence intensity of 25 μM 25% nR8-ELP nanoparticles after different incubation times represented after background correction (minimal fluorescence intensity) and normalized to maximum fluorescence intensity of the peak at 30 μm from the outer edge of the spheroid.

suggested macropinocytosis as the major endocytic pathway, as has been reported before for octa-arginine mediated uptake [36,37]. Octa-arginine by itself has little cytotoxicity, which may be attributed to the low membrane-activity of this CPP [38]. Also for ELP nanoparticles containing R8 up to a ratio of 25% R8, toxicity was low. This observation is in contrast to the multivalent presentation of nona-arginine on a linear backbone [25], demonstrating that geometry of presentation has a major impact on the toxicity of oligoarginines.

For free oligo-arginines coupled to low molecular weight cargos, a concentration-dependent, direct cytoplasmic uptake has been observed [39,40]. This uptake was even more pronounced when cyclic versions of the peptide were employed and could then be extended to low molecular weight proteins [41]. To explore the relevance of this observation for uptake of ELP-nanoparticles we also synthesized a cyclic-R8-coupled ELP version. However, as for the linear R8 coupled ELP nanoparticles, uptake was only endocytic independent of concentration (not shown). This result demonstrates that also for cyclic peptides there is a size limit to this mode of uptake.

The promotion of penetration by conjugation of R8 was not necessarily to be expected as R8 was primarily selected as a cell-penetrating peptide and the ability to induce cellular uptake was confirmed in 2D tissue cultures. Uptake of R8 is associated with binding to glycosaminoglycans [42] and this interaction has also been associated with triggering of endocytosis [43]. In our view, the best view to explain this counterintuitive finding may be that exchange between glycosaminoglycans between adjacent cells is faster than induction of endocytosis.

To describe the penetration of high-affinity binders into three-dimensional tissues, the concept of the binding site barrier has been formulated. Even though the affinity of individual CPPs for glycosaminoglycans is only in the upper nanomolar range [44–46], the multivalent display on the surface of particles can strongly increase affinity through avidity effects [25]. We addressed the potential presence of a binding site barrier by varying the density of the CPP as well as the concentration of the ELP nanoparticles. The first intervention affected the avidity, and both should promote the saturation of binding sites. After normalization of the fluorescence intensities, penetration was independent of peptide density. There was, however, a concentration dependence. For 2.5 μM ELP-nanoparticles, also after 24 h fluorescence was restricted to the periphery of the spheroids. In contrast, for 10 μM and 25 μM ELPs, efficient penetration to the same degree was observed. Further support for the presence of a binding site barrier came from an experiment in which we incubated spheroids for a 30 min pulse followed by a 24 h chase. No spreading of fluorescence from the brightly fluorescent rim at the periphery of the spheroids could be observed (not shown). The observation that ELP nanoparticles not carrying any R8 did not show any penetration suggests that the binding site barrier is a consequence of uptake rather than saturation of binding sites on the glycosaminoglycans. At higher concentrations the endocytic capacity may become increasingly exhausted. Rapid exchange between a bound and unbound state should promote percolation of the particles through the interstitial space. Apparently, even with an avidity effect in place,

the interaction with the glycocalyx still has a high enough off-rate.

Also outside the field of cell-penetrating peptides, positive charge has been demonstrated to enhance penetration. For dendrimers that were significantly smaller than the ELP-nanoparticles, positively charged terminal groups provided increased tumor penetration compared to neutral or negatively charged terminal groups [47]. Regardless of this addition, smaller dendrimers seemed to penetrate more quickly. Addition of R8 to somewhat larger dendrimers significantly boosted the penetration [48]. Also for lipid nanoparticles similar observations were made [49,50]. However, in these and other studies penetration was inferred at best from confocal images of uncleared spheroids so that in fact, no information on penetration behavior could be derived [51,52]. With the use of cleared and sectioned spheroids, we quantified the cellular uptake and 3D penetration of R8-conjugated ELP-nanoparticles to disclose the CPP's role as dual functionality charge carrier. Spheroids are a decisive but only first step towards physiologically more relevant tumor models and it will be interesting to investigate penetration as a function of cell type and spheroid size. Furthermore, it will be interesting to extend these studies to models that also incorporate perfusion and extracellular matrix [53].

Surprisingly, starting after 4 h fluorescence in the periphery decreased. By comparison, it still increased in the central parts of the spheroids. A possible explanation could be degradation of ELP-nanoparticles. In this case, however, ELP-nanoparticles that were only externally associated with the cells in the periphery still had to diffuse further towards the center. Alternatively, the extended presence of R8-ELP nanoparticles could lead to a dissociation of cells from the periphery, a hypothesis that is supported by the rugged appearance of spheroids after a 48 h incubation. Further research will be required to address how *in vivo* heterogeneity in the composition of the extracellular matrix, presence of different cell types and interstitial fluid pressure affect particle penetration [53]. In addition, the formation of a protein corona surrounding the nanoparticles could influence penetration and accumulation [54].

ELP-based nanoparticles are being pursued as a strategy for targeted drug delivery and represent excellent candidates for this purpose because of their biodegradability, biocompatibility, and the presence of both hydrophobic and hydrophilic components in the same system that provide flexibility in drug formulation [5]. Moreover, proteins can be easily extended with targeting moieties such as nanobodies [19], and also variation of the CPP may further tune penetration [55]. This study was primarily conceptional in nature, demonstrating that a CPP combined two functionalities, which are cell uptake and penetration, in one moiety. For future therapeutic applications, is has already been shown for ELP conjugates with the photosensitizer IRDye700DX, that activity in 2D tissue cultures can be obtained at picomolar concentrations. However, as concentrations up to 25 μM were well tolerated, for drug-conjugated ELPs significant payloads can be delivered [19]. Mixing of ELPs carrying different functionalities allows for a flexible adjustment of the density of the delivery moiety. It will be highly interesting to which degree the combination of CPP-conjugated ELPs with ELPs carrying receptor-specific targeting ligands will enable a fine-tuning of activities mediating uptake and targeting.

## 4. Materials and methods

***Materials*** – All chemicals were purchased from Sigma-Aldrich (Zwijndrecht, The Netherlands) unless stated otherwise.

***Recombinant design of ELP constructs*** – The gene sequences coding for all ELP constructs were cloned into pET-24a(+) (Novagen, Amsterdam, The Netherlands) expression vectors, transformed into E.coli BLR(DE3) (Novagen) cells and grown on agar plates containing 30 μg/mL kanamycin overnight at 37 °C. A single colony was grown overnight at 30 °C, 250 rpm in LB medium containing 50 μg/mL kanamycin and 0.5% w/v D-glucose. The overnight culture was diluted to an $OD_{600}$ of 0.1 in filter-sterilized AIM TB medium (Formedium, Hunstanton, UK) containing 6 g/L glycerol, 0.005% Antifoam 204 and 50 μg/mL kanamycin. Cells were grown at 300 rpm at 37 °C for 20 h. For constructs containing R8, the culture was shifted to 30 °C after 4 h of growth.

***ELP purification*** – Cells were collected by centrifugation at 2000*g*, 4 °C for 30 min. For cytoplasmic extraction, 1 g of wet cell pellet was resuspended in 2 mL lysis buffer (50 mM Tris-HCl pH 8.0, 25 mM NaCl, 1 mM EDTA, 0.1 mM PMSF, Complete Protease Inhibitor Cocktail (1 tablet/50 mL, 0.5 mg/mL lysozyme) and incubated for 4 h at 4 °C. Lysis was followed by sonication on a Branson Sonifier 250 (power level 2–4, 12 cycles of 10 s sonication, 10 s breaks). Cell debris was collected by centrifugation at 15,000*g*, 4 °C for 15 min. Residual DNA was precipitated by adding 0.5% w/v polyethylenimine and removed by centrifugation at 15,000*g*, 4 °C for 15 min. ELPs were precipitated by adding a saturated solution of $(NH_4)_2SO_4$ up to 10–25 v/v %, depending on protein concentration. Proteins were collected ('hot spin') by centrifugation at 15,000*g* at 4 °C for 15 min. The pellet was resuspended in phosphate buffered saline and centrifuged to remove insoluble contaminants at 15,000*g*, 4 °C for 20 min ('cold spin'). The cycles of 'hot' and 'cold' spins were repeated until sufficient purity was achieved, usually after 2–4 cycles. ELPs were resuspended in MilliQ, desalted on a HiPrep 26/10 column (GE Healthcare Life Sciences, Eindhoven, The Netherlands) with an AKTA Explorer 10 (GE Healthcare Life Sciences) at 1 mL/min MilliQ. Residual salt concentration was below 0.001 mg/mL as determined by conductivity. The ELP solution was filter-sterilized with 0.22 μm PES syringe filters (Nalgene) and freeze-dried. Yield was determined by weighting and varied around 20–200 mg/L culture.

***Fluorophore conjugation*** – 3.86 mg freeze-dried ELPs were resuspended in 50 mM $NaHCO_3$, pH 7.8. 100 μg AlexaFluor647-NHS ester was dissolved in DMSO and added drop-wise to the protein solution to a stoichiometric ratio of 1 to 1. The reaction was allowed to proceed for 4 h at 21 °C, 300 rpm. Unreacted dye was removed by dialysis against MilliQ using 10 kDa MWCO Amicon Ultra-0.5 spin filter units (Millipore, Amsterdam, The Netherlands). The volume of the dialyzed protein samples was determined; efficiency of conjugation was determined by measuring dye concentration and weighing protein samples after freeze-drying. Concentration of dye was determined at 650 nm ($\varepsilon$ = 270,000 $cm^{-1} M^{-1}$) and the molecular mass was confirmed by ESI TOF. Coupling efficiency ranged from 60 to 95%.

***Electrospray ionization – time-of-flight mass spectrometry (ESI-TOF)*** – Mass was determined by ESI-TOF on a JEOL AccuTOF (JEOL, Freising, Germany). Freeze-dried samples were resuspended in MilliQ to a concentration of 10 μM. Samples were acidified with 0.1% formic acid upon injection. Deconvoluted spectra were obtained using MagTran 1.03 b2.

***Dynamic light scattering*** – Samples were diluted to a final concentration of 10 μM in PBS. Measurements were performed on a Malvern Zetasizer Nano (Sysmex, Etten-Leur, The Netherlands). Samples were incubated for 5 min at 37 °C before data collection. Reported values are averages of 3 independent measurements.

***Spectroscopy*** – Freeze-dried samples were resuspended in PBS to a concentration of 10 μM. Absorbance at 350 nm was measured on a JASCO V630 spectrophotometer (JASCO, Pfungstadt. Germany) with a cuvette path length of 1 mm. Temperature cycling was performed with a ramp rate of 0.2 °C/min.

***Cell culture*** – Primary human skin fibroblasts were obtained following informed parental consent and according to the relevant Institutional Review Boards from skin biopsies of one healthy subject (C5120). Fibroblasts were cultured in medium 199 (M-199) with Earle's Salts, L-Glutamine, 25 mM HEPES, L-Amino Acids and Phenol Red (GIBCO, Life Technologies Invitrogen, Breda, The Netherlands) supplemented with 10% (v/v) fetal calf serum (FCS) (GIBCO) in a humidified atmosphere of 95% air – 5% $CO_2$ at 37 °C.

***Confocal microscopy of uptake of ELP nanoparticles in a cell monolayer*** – One day prior to imaging, primary human skin fibroblasts were seeded at 40,000 cells/well on an 8-well coverglass slide (Nunc

Lab-Tek Chamber slide #1.0 Borosilicate coverglass, Nunc, Wiesbaden, Germany). On the day of imaging, the medium was replaced by serum-containing medium containing 10 μM ELP nanoparticles (concentration refers to ELP) labeled with 5% Alexa$^{647}$-peptides including various fractions (0–25%) of R8-ELP for an incubation time of 1, 2, 4 or 24 h. After incubation, the medium including particles was removed and the cells were washed three times with PBS and imaged in M-199 with Earl's Salts, L-Glutamine, 2.2 g/L sodium bicarbonate and without phenolred (GIBCO), supplemented with 10% (v/v) FCS.

CellMask Green (Life Technologies Invitrogen) was used to stain the plasma membranes. Cells were incubated with the 1x working solution (provided solution is 1000 ×) for three minutes, washed three times with PBS and imaged within 10 min in M-199 without phenolred, to prevent redistribution of the dye into the cytoplasm.

To stain the lysosomes, the cells were incubated with 50 nM LysoTracker Green DND-26 (Thermo Fisher Scientific) for one hour. After staining, the cells were washed three times with PBS and imaged in M-199 without phenolred.

Imaging was performed with a TCS SP5 confocal microscope (Leica Microsystems, Mannheim, Germany) equipped with an HCX PL APO 63x N.A. 1.2 water immersion objective. Cells were maintained at 37 °C on a temperature-controlled microscope stage. The ELP nanoparticles labeled with Alexa$^{647}$ were excited with a 633 nm HeNe laser and emission was collected between 655 and 750 nm. The green co-localization markers (CellMask Green, LysoTracker Green) were excited by an argon laser at 488 nm and emission was collected between 500 and 550 nm. The obtained images were further processed using FIJI (http://fiji.sc/).

***Flow cytometry*** – Human primary skin fibroblasts were seeded in 24-well plates (Sarstedt, Numbrecht, Germany) one day (80,000 cells/well) or two days (40,000 cells/well) prior to measurement. Cells were incubated with the indicated concentration of ELP nanoparticles for two hours. After incubation, the cells were washed with PBS and cells were detached by trypsinisation for 5 min, spun down and resuspended in 100 μL M-199 without phenolred. The fluorescent signal of the nanoparticles was measured using a FACSCalibur flow cytometer (BD BioSciences, Erembodegem, Belgium) and subsequently data was analyzed with Flowing Software (http://www.uskonaskel.fi/flowingsoftware/). The cells were gated on the live population by forward and sideward scatter and 10,000 cells were counted to determine cellular nanoparticle uptake by measure of mean cellular fluorescence.

***Inhibition of endocytic pathways*** – To study the contribution of endocytic pathways responsible for uptake of ELP nanoparticles, primary human skin fibroblasts were incubated with either 50 μM 5-(N-ethyl-N-isopropyl)amiloride hydrochloride, 50 μM monodansyl-cadaverine, and 100 μM genistein to inhibit macropinocytosis, clathrin-mediated endocytosis and caveolae-mediated endocytosis, respectively, followed by two hours incubation with the ELP nanoparticles (10 μM). Cell-associated fluorescence was measured by flow cytometry as described above.

***Cell death assay*** – Toxicity of ELP nanoparticles with different fractions of R8-ELP (0–90%) was evaluated after 24 h using the propidium iodide assay. Two days prior to measuring cell death, 40,000 cells were seeded in 24-well plates (Sarstedt). The following day, cells were incubated with a range of concentrations (0–100 μM) of ELP nanoparticles. After 24 h of incubation, the cell medium was collected, the cells were washed three times with PBS, then trypsinized and spun down. Subsequently, the cells were resuspended and incubated for 30 min at 4 °C with 100 μL Nicoletti buffer (0.1% $Na_3C_6H_5O_7$, 50 μg/mL propidium iodide, 0.01% Triton X-100) and no less than 10,000 cells were measured with flow cytometry to determine cell death.

***Formation of spheroids*** – Human glioblastoma cells (U-87) (gift from Dr. Joost Schalkwijk, Department of Dermatology, RIMLS, Radboudumc, Nijmegen) were cultured in Dulbecco's Modified Eagle's Medium (DMEM) containing 4.5 g/L D-glucose, GlutaMAX and pyruvate (GIBCO) and supplemented with 10% (v/v) FCS (GIBCO) in a humidified atmosphere of 95% air – 5% $CO_2$ at 37 °C. Spheroids were formed by plating 100 μL of a 10,000 cell/mL single cell suspension of U-87 cells onto agarose (Sigma) (0.75% (w/v) in PBS) coated 96-well plates (Corning). Cells were allowed to aggregate for 5 days without motion, resulting in the formation of a single spheroid per well. On day 5, the spheroids were incubated with the appropriate concentration of ELP nanoparticles for the indicated incubation times. After incubation, the spheroids were washed three times with PBS. Subsequently, the spheroids were fixed in paraformaldehyde (Sigma) (4% (v/v) in PBS). After fixation, the spheroids were carefully cut in half with a sharp razor blade and placed with the flat side (inner half) on a coverslip in a drop of gelatin (4% (w/v in PBS). Nuclei were stained with DAPI (ThermoFisher Scientific), and the actin filaments with Alexa$^{488}$ phalloidin (ThermoFisher Scientific).

Clearing was performed based on a protocol adapted from Ke et al. [35]. A 115% w/v fructose stock solution was prepared by dissolving fructose (Sigma) in MQ for 30 min at 80 °C under stirring. Three solutions were prepared (28.75% w/v, 57.5% w/v, and 115% w/v) and 0.5% v/v 1-thioglycerol was added to all solutions. Cells were incubated with 200 μL preheated (60 °C) fructose solutions in ascending order, each for 1 h at RT. Spheroids were imaged in 115% w/v fructose in an 8-well coverglass slide.

The HeLa T-Rex Flp-in cell line (a kind gift of Dr. Stephen Taylor, Faculty of Life Science, Manchester, United Kingdom) stably expressing COX8-AcGFP1 [56] was cultured in Dulbecco's Modified Eagle's Medium (DMEM) containing 4.5 g/L D-glucose, GlutaMAX and pyruvate (GIBCO), supplemented with 10% (v/v) fetal bovine serum (GIBCO), 1% (v/v) penicillin/streptomycin (GIBCO), 4 μg/mL blasticidin (GIBCO), 200 μg/mL hygromicin (Invitrogen) in a humidified atmosphere of 95% air, 5% $CO_2$ at 37 °C. To induce expression of COX8-AcGFP1, 1 μg/mL doxycyclin was added to the medium. Spheroids were formed by plating 200 μL of a 12,500 cell/mL single cell suspension of HeLa-AcGFP1 onto agarose (0.75% (w/v) in PBS) coated 96-well plates (Corning). Cells were allowed to aggregate for 4 days without motion, resulting in the formation of a single spheroid per well. On day 4, the spheroids were fixed and cut, or cleared as described above prior to confocal imaging.

***Confocal microscopy of spheroids*** – Imaging of spheroids was performed using a TCS SP5 confocal microscope equipped with an HC PL FLUOTAR 20x N.A. 0.5 dry objective. The ELP nanoparticles labeled with Alexa$^{647}$ were excited with a 633 nm HeNe laser and emission was collected between 655 and 750 nm. The COX8-AcGFP1 construct expressed in the HeLa cells was excited by an argon laser at 488 nm, and emission was recorded between 500 and 550 nm. The samples co-stained with DAPI (Life Technologies) (excited with a 405 nm diode laser) and Alexa$^{488}$ phalloidin (Life Technologies) were imaged with a Zeiss LSM510 META confocal microscope (Carl Zeiss, Sliedrecht, The Netherlands) using a 63x oil immersion objective (N.A. 1.4). Images were analyzed with Image Pro Plus 6.1 (Media Cybernetics, Rockville, MD, USA) and FIJI.

***Statistical Analysis –*** The number of independent experiments is marked by n, each experiment was performed in duplicate. Average values are represented as mean ± SD. Values were tested for significance using the two-way analysis of variance (ANOVA) at 95% confidence level ($p < 0.05$), followed by Tukey's multiple comparisons test (Graph Pad Prism software, version 6), unless stated otherwise. Significant differences are indicated by $^{*}P < 0.05$, $^{**}P < 0.01$, $^{***}P < 0.001$, $^{****}P < 0.0001$.

## Acknowledgements

This research was financially supported by the Radboud Nanomedicine Alliance and the Ministry of Education, Culture and Science (Gravitation Program 024.001.035). The authors acknowledge Huib Croes for his assistance in fixation and sectioning of spheroids.

## Conflict of Interest

This research was carried out in a collaborative project with Khondrion BV (a Radboud University Medical Center spin-off biotech company). J.A.M.S. is the founding CEO of Khondrion BV. P.H.G.M.W. and W.J.H.K. are scientific advisors for Khondrion BV. W.J.H.K. is scientific advisor of Mitoconix Bio Ltd. (Ness Ziona, Israel).

## Appendix A. Supplementary material

Supplementary data to this article can be found online at https://doi.org/10.1016/j.ejpb.2019.02.010.

## References


[1] B. Felice, M.P. Prabhakaran, A.P. Rodriguez, S. Ramakrishna, Drug delivery vehicles on a nano-engineering perspective, Mater. Sci. Eng., C Mater. Biol. Appl. 41 (2014) 178–195 doi:S0928-4931(14)00241-0 [pii] 10.1016/j.msec.2014.04.049.

[2] W.B. Liechty, D.R. Kryscio, B.V. Slaughter, N.A. Peppas, Polymers for drug delivery systems, Annu. Rev. Chem. Biomol. Eng. 1 (2010) 149–173, https://doi.org/10.1146/annurev-chembioeng-073009-100847.

[3] B.D. Ulery, L.S. Nair, C.T. Laurencin, Biomedical applications of biodegradable polymers, J. Polym. Sci. B Polym. Phys. 49 (2011) 832–864, https://doi.org/10.1002/polb.22259.

[4] F.C.M. Smits, B.C. Buddingh, M.B. Van Eldijk, J.C.M. Van Hest, Elastin-like polypeptide based nanoparticles: design rationale toward nanomedicine, Macromol. Biosci. 15 (1) (2015) 36–51, https://doi.org/10.1002/mabi.201400419.

[5] A.O. Elzoghby, W.M. Samy, N.A. Elgindy, Protein-based nanocarriers as promising drug and gene delivery systems, J. Control. Release 161 (2012) 38–49, https://doi.org/10.1016/j.jconrel.2012.04.036.

[6] J.F. Almine, D.V. Bax, S.M. Mithieux, et al., Elastin-based materials, Chem. Soc. Rev. 39 (9) (2010) 3371–3379, https://doi.org/10.1039/b919452p.

[7] D.W. Urry, M.M. Long, B.A. Cox, T. Ohnishi, L.W. Mitchell, M. Jacobs, The synthetic polypentapeptide of elastin coacervates and forms filamentous aggregates, Biochim. Biophys. Acta - Protein Struct. 371 (1974) 597–602, https://doi.org/10.1016/0005-2795(74)90057-9.

[8] A.S.C. Soon, M.H. Smith, E.S. Herman, L.A. Lyon, T.H. Barker, Development of self-assembling mixed protein micelles with temperature-modulated avidities, Adv. Healthc Mater. 2 (7) (2013) 1045–1055, https://doi.org/10.1002/adhm.201200330.

[9] I.L. Wu, M.A. Patterson, H.E. Carpenter Desai, R.A. Mehl, G. Giorgi, V.P. Conticello, Multiple site-selective insertions of noncanonical amino acids into sequence-repetitive polypeptides, ChemBioChem. 14 (8) (2013) 968–978, https://doi.org/10.1002/cbic.201300069.

[10] N.K. Li, F.G. Quiroz, C.K. Hall, A. Chilkoti, Y.G. Yingling, Molecular description of the lcst behavior of an elastin-like polypeptide, Biomacromolecules 15 (10) (2014) 3522–3530, https://doi.org/10.1021/bm500658w.

[11] J.R. McDaniel, D.C. Radford, A. Chilkoti, A unified model for de novo design of elastin-like polypeptides with tunable inverse transition temperatures, Biomacromolecules 14 (8) (2013) 2866–2872, https://doi.org/10.1021/bm4007166.

[12] D.W. Urry, D.C. Gowda, T.M. Parker, et al., Hydrophobicity scale for proteins based on inverse temperature transitions, Biopolymers 32 (9) (1992) 1243–1250, https://doi.org/10.1002/bip.360320913.

[13] R. Saxena, M.J. Nanjan, Elastin-like polypeptides and their applications in anticancer drug delivery systems: a review, Drug Deliv. 22 (2) (2015) 156–167, https://doi.org/10.3109/10717544.2013.853210.

[14] J.S. Ryu, D. Raucher, Elastin-like polypeptide for improved drug delivery for anticancer therapy: preclinical studies and future applications, Expert Opin. Drug Deliv. 12 (2015) 653–667, https://doi.org/10.1517/17425247.2015.974546.

[15] J. Rodríguez-Hernández, F. Chécot, Y. Gnanou, S. Lecommandoux, Toward, "smart" nano-objects by self-assembly of block copolymers in solution, Prog. Polym. Sci. 30 (7) (2005) 691–724, https://doi.org/10.1016/j.progpolymsci.2005.04.002.

[16] E.R. Wright, V.P. Conticello, Self-assembly of block copolymers derived from elastin-mimetic polypeptide sequences, Adv. Drug Deliv. Rev. 54 (8) (2002) 1057–1073, https://doi.org/10.1016/S0169-409X(02)00059-5.

[17] R. Herrero-Vanrell, A.C. Rincón, M. Alonso, V. Reboto, I.T. Molina-Martinez, J.C. Rodríguez-Cabello, Self-assembled particles of an elastin-like polymer as vehicles for controlled drug release, J. Control. Release 102 (1) (2005) 113–122, https://doi.org/10.1016/j.jconrel.2004.10.001.

[18] P.C. Bessa, R. Machado, S. Nürnberger, et al., Thermoresponsive self-assembled elastin-based nanoparticles for delivery of BMPs, J. Control. Release 142 (3) (2010) 312–318, https://doi.org/10.1016/j.jconrel.2009.11.003.

[19] J. Pille, S.A.M. Van Lith, J.C.M. Van Hest, W.P.J. Leenders, Self-assembling VHH-elastin-like peptides for photodynamic nanomedicine, Biomacromolecules 18 (4) (2017) 1302–1310, https://doi.org/10.1021/acs.biomac.7b00064.

[20] F. Madani, S. Lindberg, U. Langel, S. Futaki, A. Graslund, Mechanisms of cellular uptake of cell-penetrating peptides, J. Biophys. 2011 (2011) 414729, , https://doi.org/10.1155/2011/414729.

[21] A.H. Van Asbeck, A. Beyerle, H. McNeill, et al., Molecular parameters of siRNA-cell penetrating peptide nanocomplexes for efficient cellular delivery, ACS Nano 7 (5) (2013) 3797–3807, https://doi.org/10.1021/nn305754c.

[22] S. Futaki, T. Suzuki, W. Ohashi, et al., Arginine-rich Peptides: an abundant source of membrane-permeable peptides having potential as carriers for intracellular protein delivery, J. Biol. Chem. 276 (2001) 5836–5840, https://doi.org/10.1074/jbc.M007540200.

[23] K. Koschek, M. Dathe, J. Rademann, Effects of charge and charge distribution on the cellular uptake of multivalent arginine-containing peptide-polymer conjugates, ChemBioChem. 14 (2013) 1982–1990, https://doi.org/10.1002/cbic.201300365.

[24] R. Wallbrecher, W.P. Verdurmen, S. Schmidt, et al., The stoichiometry of peptide-heparan sulfate binding as a determinant of uptake efficiency of cell-penetrating peptides, Cell. Mol. Life Sci. 71 (2014) 2717–2729, https://doi.org/10.1007/s00018-013-1517-8.

[25] A. Chakrabarti, J.J. Witsenburg, M.D. Sinzinger, et al., Multivalent presentation of the cell-penetrating peptide nona-arginine on a linear scaffold strongly increases its membrane-perturbing capacity, Biochim. Biophys. Acta – Biomembr. 1838 (2014) 3097–3106, https://doi.org/10.1016/j.bbamem.2014.08.001.

[26] T.T. Goodman, P.L. Olive, S.H. Pun, Increased nanoparticle penetration in collagenase-treated multicellular spheroids, Int. J. Nanomed. 2 (2007) 265–274 https://www.ncbi.nlm.nih.gov/pubmed/17722554works.

[27] T.T. Goodman, J. Chen, K. Matveev, S.H. Pun, Spatio-temporal modeling of nanoparticle delivery to multicellular tumor spheroids, Biotechnol. Bioeng. 101 (2008) 388–399, https://doi.org/10.1002/bit.21910.

[28] M. Juweid, R. Neumann, C. Paik, et al., Micropharmacology of monoclonal antibodies in solid tumors: direct experimental evidence for a binding site barrier, Cancer Res. 52 (1992) 5144–5153.

[29] T. Saga, R.D. Neumann, T. Heya, et al., Targeting cancer micrometastases with monoclonal antibodies: a binding-site barrier, Proc. Natl. Acad. Sci. 92 (19) (1995) 8999–9003, https://doi.org/10.1073/pnas.92.19.8999.

[30] H. Lee, H. Fonge, B. Hoang, R.M. Reilly, C. Allen, The effects of particle size and molecular targeting on the intratumoral and subcellular distribution of polymeric nanoparticles, Mol. Pharm. 7 (4) (2010) 1195–1208, https://doi.org/10.1021/mp100038h.

[31] A. Ziegler, J. Seelig, Binding and clustering of glycosaminoglycans: a common property of mono- and multivalent cell-penetrating compounds, Biophys. J. 94 (2008) 2142–2149, https://doi.org/10.1529/biophysj.107.113472.

[32] C. Riccardi, I. Nicoletti, Analysis of apoptosis by propidium iodide staining and flow cytometry, Nat. Protoc. 1 (2006) 1458–1461, https://doi.org/10.1038/nprot.2006.238.

[33] H.S. Bell, I.R. Whittle, M. Walker, H.A. Leaver, S.B. Wharton, The development of necrosis and apoptosis in glioma: experimental findings using spheroid culture systems, Neuropathol. Appl. Neurobiol. 27 (4) (2001) 291–304, https://doi.org/10.1046/j.0305-1846.2001.00319.x.

[34] G. Mehta, A.Y. Hsiao, M. Ingram, G.D. Luker, S. Takayama, Opportunities and challenges for use of tumor spheroids as models to test drug delivery and efficacy, J. Control. Release 164 (2012) 192–204, https://doi.org/10.1016/j.jconrel.2012.04.045.

[35] M.T. Ke, S. Fujimoto, T. Imai, SeeDB: A simple and morphology-preserving optical clearing agent for neuronal circuit reconstruction, Nat. Neurosci. 16 (8) (2013) 1154–1161, https://doi.org/10.1038/nn.3447.

[36] I. Nakase, M. Niwa, T. Takeuchi, et al., Cellular uptake of arginine-rich peptides: roles for macropinocytosis and actin rearrangement, Mol. Ther. 10 (2004) 1011–1022 doi:S1525-0016(04)01396-6 [pii] 10.1016/j.ymthe.2004.08.010.

[37] S.R. Macewan, A. Chilkoti, Digital switching of local arginine density in a genetically encoded self-assembled polypeptide nanoparticle controls cellular uptake, Nano Lett. 12 (2012) 3322–3328, https://doi.org/10.1021/nl301529p.

[38] G. Tünnemann, G. Ter-Avetisyan, R.M. Martin, M. Stöckl, A. Herrmann, M.C. Cardoso, Live-cell analysis of cell penetration ability and toxicity of oligo-arginines, J. Pept. Sci. 14 (2008) 469–476, https://doi.org/10.1002/psc.968.

[39] F. Duchardt, M. Fotin-Mleczek, H. Schwarz, R. Fischer, R. Brock, A comprehensive model for the cellular uptake of cationic cell-penetrating peptides, Traffic 8 (7) (2007) 848–866, https://doi.org/10.1111/j.1600-0854.2007.00572.x.

[40] M. Kosuge, T. Takeuchi, I. Nakase, A.T. Jones, S. Futaki, Cellular internalization and distribution of arginine-rich peptides as a function of extracellular peptide concentration, serum, and plasma membrane associated proteoglycans, Bioconjug. Chem. 19 (3) (2008) 656–664, https://doi.org/10.1021/bc700289w.

[41] N. Nischan, H.D. Herce, F. Natale, et al., Covalent attachment of cyclic TAT peptides to GFP results in protein delivery into live cells with immediate bioavailability, Angew. Chem. Int. Ed. 54 (6) (2015) 1950–1953, https://doi.org/10.1002/anie.201410006.

[42] Y. Takechi-Haraya, H. Saito, Current understanding of physicochemical mechanisms for cell membrane penetration of arginine-rich cell penetrating peptides: role of glycosaminoglycan interactions, Curr. Protein Pept. Sci. 19 (6) (2018), https://doi.org/10.2174/1389203719666180112100747.

[43] H.C. Christianson, M. Belting, Heparan sulfate proteoglycan as a cell-surface endocytosis receptor, Matrix Biol. 35 (2014) 51–55, https://doi.org/10.1016/j.matbio.2013.10.004.

[44] W.P.R. Verdurmen, P.H. Bovee-Geurts, P. Wadhwani, et al., Preferential uptake of L-versus D-amino acid cell-penetrating peptides in a cell type-dependent manner, Chem. Biol. 18 (8) (2011) 1000–1010, https://doi.org/10.1016/j.chembiol.2011.06.006.

[45] E. Gonçalves, E. Kitas, J. Seelig, Structural and thermodynamic aspects of the interaction between heparan sulfate and analogues of melittin, Biochemistry 45 (9) (2006) 3086–3094, https://doi.org/10.1021/bi052221t.

[46] F. Duchardt, I.R. Ruttekolk, W.P.R. Verdurmen, et al., A cell-penetrating peptide derived from human lactoferrin with conformation-dependent uptake efficiency, J. Biol. Chem. 284 (52) (2009) 36099–36108, https://doi.org/10.1074/jbc.M109.

036426.
[47] J. Bugno, H.J. Hsu, R.M. Pearson, H. Noh, S. Hong, Size and surface charge of engineered poly(amidoamine) dendrimers modulate tumor accumulation and penetration: a model study using multicellular tumor spheroids, Mol. Pharm. 13 (7) (2016) 2155–2163, https://doi.org/10.1021/acs.molpharmaceut.5b00946.
[48] S.V.K. Rompicharla, P. Kumari, B. Ghosh, S. Biswas, Octa-arginine modified poly (amidoamine) dendrimers for improved delivery and cytotoxic effect of paclitaxel in cancer, Artif. Cells, Nanomed. Biotechnol. (2018) 1–13, https://doi.org/10.1080/21691401.2018.1470527.
[49] R. Ran, H. Wang, Y. Liu, et al., Microfluidic self-assembly of a combinatorial library of single- and dual-ligand liposomes for in vitro and in vivo tumor targeting, Eur. J. Pharm. Biopharm. 130 (2018) 1–10, https://doi.org/10.1016/j.ejpb.2018.06.017.
[50] Y. Yang, Y. Yang, X. Xie, X. Cai, X. Mei, Preparation and characterization of photo-responsive cell-penetrating peptide-mediated nanostructured lipid carrier, J. Drug Target. 22 (10) (2014) 891–900, https://doi.org/10.3109/1061186X.2014.940589.
[51] H. Gao, Q. Zhang, Y. Yang, X. Jiang, Q. He, Tumor homing cell penetrating peptide decorated nanoparticles used for enhancing tumor targeting delivery and therapy, Int. J. Pharm. 478 (1) (2015) 240–250, https://doi.org/10.1016/j.ijpharm.2014.11.029.
[52] X. He, X. Chen, L. Liu, et al., Sequentially triggered nanoparticles with tumor penetration and intelligent drug release for pancreatic cancer therapy, Adv. Sci. 5 (5) (2018), https://doi.org/10.1002/advs.201701070.
[53] D. Van Den Brand, L.F. Massuger, R. Brock, W.P.R. Verdurmen, Mimicking tumors: toward more predictive in vitro models for peptide- and protein-conjugated drugs, Bioconjug. Chem. 28 (3) (2017) 846–856, https://doi.org/10.1021/acs.bioconjchem.6b00699.
[54] K. Huang, R. Boerhan, C. Liu, G. Jiang, Nanoparticles penetrate into the multicellular spheroid-on-chip: effect of surface charge, protein corona, and exterior flow, Mol. Pharm. 14 (12) (2017) 4618–4627, https://doi.org/10.1021/acs.molpharmaceut.7b00726.
[55] D. van den Brand, C. Veelken, L. Massuger, R. Brock, Penetration in 3D tumor spheroids and explants: adding a further dimension to the structure-activity relationship of cell-penetrating peptides, Biochim. Biophys. Acta – Biomembr. 1860 (6) (2018) 1342–1349, https://doi.org/10.1016/j.bbamem.2018.03.007.
[56] C.E.J. Dieteren, P.H.G.M. Willems, R.O. Vogel, et al., Subunits of mitochondrial complex I exist as part of matrix- and membrane-associated subcomplexes in living cells, J. Biol. Chem. 283 (50) (2008) 34753–34761, https://doi.org/10.1074/jbc.M807323200.